Optimization of microstructured hollow fiber design for membrane distillation applications using CFD modeling

Xing Yang[1,2], Hui Yu[1,2,3], Rong Wang*[,1,2], Anthony G. Fane[1,2]

1. Singapore Membrane Technology Centre, Nanyang Technological University, Singapore 639798
2. School of Civil and Environmental Engineering, Nanyang Technological University, Singapore 639798
3. School of Chemical Engineering, Sichuan University, China 610065

*Corresponding author at: School of Civil and Environmental Engineering,
Nanyang Technological University, 639798 Singapore,
Singapore. Tel.: +65 6790 5327; fax: +65 6791 0676.
E-mail address: rwang@ntu.edu.sg (R. Wang).

Abstract

This study explores the potential of microstructured hollow fiber designs to enhance process performance in a direct contact membrane distillation (DCMD) system. Hollow fibers with ten different geometries (wavy and gear-shaped cross sections) were evaluated. A series of three dimensional computational fluid dynamic (CFD) simulations were carried out to investigate their capability in terms of depolarizing the buildup of liquid boundary layers, thus improving water productivity.

Analyses of heat and mass transfer as well as the flow-field distribution in respective MD modules were obtained. It was found that the enhancement of the heat-transfer coefficients, h_f, was up to 4.5-fold for a module with a wavy fiber design 07 and an approximate 5.5-fold h_p increase for a gear-shaped fiber design. The average temperature polarization coefficient and mass flux N_m of the gear-shaped fiber module showed an improvement of 57 % and 66 %, respectively, over the original straight fiber design, followed by the wavy designs 07 and 08. The enhanced module performance was attributed to the improved hydrodynamics through the flow channels of various fiber geometries, which was confirmed by the visualization of flow-field and temperature profiles in CFD. Investigations of the fiber-length effect showed that the gear-shaped fiber modules exhibited the highest flux enhancement of 57–65 % with the same length, compared to the modules with original straight and wavy fibers.

In addition, the gear-shaped fiber module is very sensitive to feed velocity changes. Therefore, employing a smart microstructured design on the membrane surface would bring in a significant improvement under adverse flow conditions. Moreover, the computed water production and hydraulic energy consumption (*HEC*) among the modules with various fiber geometries were compared. With 1.9-fold surface area increase per unit volume, the gear-shaped fiber configuration had the highest water production but the lowest *HEC*, followed by wavy designs 07 and 08.

Key words: membrane distillation, computational fluid dynamics, microstructured fiber geometry, heat transfer, temperature polarization, process enhancement

1. Introduction

As a hybrid process of membrane separation and conventional distillation, membrane distillation (MD) is considered as a promising alternative technology for desalination to obtain clean water when waste-heat or low grade heat are available. It is a combined mass- and heat-transfer process, where the driving force is the vapor pressure gradient (due to the temperature difference) across the membrane wall. The membrane material itself should be sufficiently hydrophobic to separate the feed (hot) and permeate (cold) streams, as well as to prevent pore-wetting problems. In the configuration of direct contact MD (DCMD), the mass and heat transfers take place in three steps: water molecules in the hot stream first evaporate at the mouth of the membrane pores, then the vapor flows through the membrane matrix until condensation takes places on the cold permeate surface. As a result, high-purity water is generated. Having been studied for over 3 decades, MD is of great interest due to the benefits of moderate operating temperature, acceptable permeation rate and high salt rejection. However, industrial applications of MD remain limited due to the following technical challenges [1, 2]: difficulties in fabricating suitable MD membranes for high water permeation flux and prevention of pore wetting; relatively high thermal energy consumption (with the access to low great heat), and poor flow hydrodynamics and/or severe temperature polarization (TP) effects that compromises module performance [3, 4].

In MD, the membrane structure and material properties contribute to the permeation rate, wetting resistance as well as the TP effect. Therefore, a surge of studies in recent years have focused on membrane development [5-9], with special interest in hollow fibers due to their high surface area and modular versatility[3]. Although a few highly permeable hollow fiber membranes with large MD coefficients are available [7, 10-15], the development of MD membranes are still constrained by the conventional spinning methods and the limitation of suitable material properties. Also, the advantages of highly permeable fibers are often compromised by the morphological defects, weak mechanical strength and unsustainable long-term performance [11].

On the other hand, many studies have also focused on strategies to improve the MD performance through optimizing operation parameters [9, 16-20] and designing novel membrane modules [21-23] to alleviate the TP phenomenon and enhance permeation flux. It is shown that by incorporating proper flow alteration aids such as channeled design, external spacers or baffles into module designs, secondary flows or eddies are created. As a result, the MD flux can be greatly enhanced and the TP phenomenon can be mitigated [1, 9, 16-19, 24-29].

Another area that has been investigated for improved module performance is the microstructured surface design of the hollow fiber membranes. Inspired by the concept of corrugated surface adopted in heat-exchangers to enhance flow hydrodynamics, novel hollow fibers with modified surface geometries have been fabricated using specially designed spinnerets [30, 31]. It was reported that hollow fibers with modified surface geometries such as gear or flower shapes in cross-section have greatly improved membrane filtration performance by not only allowing a 5 or 6-fold increase of surface area and hence significant water flux enhancement, but also acting as turbulence promoters and improving anti-fouling performance for submerged membrane bioreactors (MBR) and ultrafiltration modules [32-36]. In spite of the potential benefits for creating similar improvement in a combined mass- and heat-transfer process, no related work has been done for MD applications.

In parallel with extensive experimental studies to investigate the hydrodynamics in membrane modules, computational fluid dynamics (CFD) modeling has also been widely adopted to simulate and analyze fluid dynamic behaviors in membrane processes [37, 38]. With the visualization of the flow-field (including velocity, pressure, temperature and concentration profiles) at any locations in a defined flow channel, CFD modeling can be used to correlate the fundamental mass- and heat-transfer performance with flow hydrodynamics. Therefore, it has become a valuable evaluation tool for industrial applications. Nevertheless, the CFD simulations of the MD process have been greatly limited due to the complex coupling of mass and heat transfer across bulk fluids and the membrane matrix. Mostly, simplified mathematical models were used in prior MD modeling work [37]. For instance, simulations of the feed, permeate and membrane were often treated as a conjugate problem to obtain velocity and temperature fields; while the solute transport and latent heat induced by evaporation were ignored [39, 40]. To date, the CFD work on hollow fiber MD modules is sparsely reported [38, 41]. A recent CFD study, which proposed an improved heat-transfer model to couple the latent heat to the energy conservation equation and combine it with the Navier-Stokes equations, was performed by our group to address the transport relationships between the fluids (feed and permeate) and the membrane in a single-fiber MD module [38]. The model has also been used to analyze the effectiveness of different process enhancement strategies by identifying the controlling local resistances in MD under various circumstances [41, 42].

The present work aims to evaluate the performance of a shell-side feed DCMD system with nine different types of modified fiber geometries via three dimensional (3D) CFD modeling. Since the gear- or flower-shaped fibers were comprehensively studied experimentally by others [30, 31], the current study mainly discusses the wavy microstructure and only one specific gear-shaped design. The following aspects have been investigated computationally: (1) optimization of fiber geometric structures in terms of main MD process metrics and flow-field and temperature distributions; (2) investigations of the length effect of modules with original straight, optimized wavy and gear-shaped fibers; (3) effect of flow conditions on the performance of the modules with original straight and modified fibers; (4) comparison of membrane area, water production and hydraulic energy consumption (*HEC*) among modules with various micro-structured fibers using the original design as a benchmark.

2. Theory

2.1 Geometric structures and CFD modeling methods

3D models were developed using the commercial software Fluent 6.3 to study the hydrodynamic behavior and heat transfer characteristics of ten modules with original straight and modified fibers of various surface geometries.

All the modules have the same cylindrical housings. Except for the original straight fibers, modified fibers were designed to have regularly distanced waves with a constant wall thickness or gear-like (cross-section) structure on the outer surface. The assumed dimension ns of these single-fiber modules are 0.25−0.84 m in length and 0.0095 m in shell diameter.

For the convenience of CFD modeling, the geometries were assumed to be ideal axially-symmetric structures. Hence, a series of geometric structure for 3D computing domains were built using Gambit 2.4.6 for half of the actual modules, whose mirrored images of cross-sectional structures (within a length range of 0.015 m with respect to the overall length of 0.25 m) are shown in Fig. 1 (a); while Fig. 1 (b) shows a local domain amplification to specify the dimensional parameters of these wavy microstructures, in which R_{mi} and R_{mo} are the inner and outer radii of the fiber, Δx and Δy are the cross-sectional dimensions of a wave in x and r (from the baseline to the conic peak) directions; Lx is the interval between two waves; b is the shape parameter, which represents the shape of the conic wave. To clearly show the structures of these configurations, Fig. 2 depicts the 3D schematics of single-fiber modules containing fibers of a representative wavy design and gear-shaped, respectively. In all modules, the feed and permeate streams flow through the shell and lumen of the fiber, respectively, in a counter-current mode. The dimensional specifications and respective actual outer surface area A_s (taking into account the surface corrugation) of these modified fiber geometries are given in Table 1, which shows that both wavy designs 02 and 03 have a 3.6-fold area increase compared to the original fiber; while the gear-shaped fiber gains 1.9-fold increase.

With the geometries structured, CFD simulations were carried out using Fluent. A coupled heat-transfer model was built to combine the latent heat induced by evaporation/condensation on the membrane surfaces into the MD process. Nevertheless, the influence of the normal mass flow across the membrane matrix was ignored due to a negligible contribution from the MD mass flux in a single module [38]. Based on the governing transport equations and boundary conditions involved in the simulating process discussed in a previous study [38], a brief summary is given in Table 2. It includes mathematical models, boundary conditions and modeling algorithms. In this study, a laminar model is used for simulating the original module operated under laminar operating conditions (Re < 2000); while a realizable k-ε method is applied for the original module under turbulent conditions (Re>2000) or configurations with modified fibers.

In addition, it is assumed that all nine modified fibers have the similar membrane characteristics (i.e., wall thickness, porosity, and pore size/pore size distribution, etc) as the original fiber but with different surface geometries [38]. Also, the module specifications and the operating conditions are the same as used previously [38]. The heat-transfer model has been verified previously [38, 41, 42],based on an established DCMD system for a series of experimental settings, including various feed inlet temperatures, fiber lengths and flow velocities, and modified module configurations with external aids. Based on our previous verification results, the comparisons between the CFD simulation results and experimental data of mass flux (N_m) and feed pressure drop (ΔP_f) showed good agreement with small relative errors of ±5 %. Hence, the model verification shall not be repeated here.

2.2 Computational domain and grid structures

As mentioned previously, the geometric structures of ten single-fiber modules with original straight and modified fibers were created in this study using the Gambit software. A combination of tetrahedral and hexahedral girds was adopted to generate meshes within the calculating domains for all configurations. The grid number was optimized using the grid independence tests. In the radial r direction, a grid scale of 5×10^{-6} m was chosen for the bulk permeate and membrane, and progressively increased scales from 5×10^{-6} to 2×10^{-4} m were set for the bulk feed (shell-side); while in the axial x direction, a grid scale of 1×10^{-4} m was employed. A local mesh structure of a modul e with straight fibers is shown in Fig. 3. It is noted that the effect of the hollow fiber membrane surface roughness on the wall boundary conditions was ignored due to its much smaller scale than that of a mesh element. The iteration criterion for convergence is 10^{-5} in Fluent.

2.3 Heat-transfer analysis of MD process

As the influence of the normal mass transferred across the membrane matrix was ignored due to the negligible amount, the corresponding induced latent heat was treated as a MD characteristic and coupled into the heat-transfer model during the simulations [41]. The MD heat transport is often elucidated in three steps, and the overall heat-transfer rate through the membrane, Q, consists of the latent heat Q_{MD} (evaporation) and heat loss Q_{HL} (conduction). The respective heat-transfer coefficients of the feed h_f, the permeate h_p and the membrane h_m can be calculated based on the temperature profiles provided by CFD simulations. The main heat-transfer equations and definitions and equations required for data post-processing are summarized in Table 3.

In Table 3, the MD coefficient C and solution temperatures (vapor pressure) given in Eq. (5) both contribute to the permeation flux N_m. Based on the prior studies, the C is an intrinsic mass-transfer coefficient of the membrane [43] and is calculated based on a combination of structural parameters (thickness, porosity, pore size and pore size distribution) [42]. Therefore, in the current study a general C value for the selected original straight and wavy designs is determined as 8.0×10^{-7} kg m^{-2} s^{-1} Pa^{-1}; while due to the slight variation of thickness, the gear-shaped fiber has a modified value C^{*} of 6.4×10^{-7} kg m^{-2} s^{-1} Pa^{-1} with fixed membrane matrix structure (where $C^{*} = (0.6+0.4\ (\delta_m/\delta_m^{*}))C$, with the original $\delta_m = 0.27$ mm and modified $\delta_m^{*} = 0.52$ mm, as shown in Fig. 2(b)). As important MD performance metrics, the temperature-polarization coefficient (*TPC*) and hydraulic energy consumption (*HEC*) can be calculated based on Eqs. (9) and (10), respectively. The *TPC* characterizes the actual driving force of the system [3]; while the *HEC* (J kg^{-}1) and water production (kg day^{-1}) are used to assess the performance of these microstructured fibers in terms of the pumping electricity cost and water production.

3. Results and discussion

3.1 Optimization of fiber geometric designs in DCMD

3.1.1 Improvement of heat transfer coefficients

Based on an analysis of the controlling heat-transfer resistance in different MD systems, external hydrodynamic aids can be employed to achieve a significant enhancement when the heat transfer through the liquid-boundary layers plays a dominant role [42]. Hence, in this study, a similar DCMD system [highly permeable membrane with membrane coefficient $C = 8.0\times10^{-7}$ kg m^{-2} s^{-1} Pa^{-1} and C^{*}(gear) = 6.4×10^{-7} kg m^{-2} s^{-1} Pa^{-1}, and relatively low operating temperatures $T_f = 327.15$ K, $T_p = 293.85$ K] was selected to investigate the effectiveness of hydrodynamic improvement by incorporating modified fibers with various surface microstructures. To optimize the fiber geometry particularly for MD applications, nine different microstructures listed in Table 1 were simulated, and Fig. 4 shows the distributions of the simulated heat transfer coefficients at the feed and permeate sides, h_f and $h_{p,}$ along the fiber length L, respectively, for single-fiber modules with the original and nine modified fibers.

In Fig. 4 (a) the h_f distribution curves for all fiber geometries show a general decreasing trend along the fiber length L. For the original module, the highest h_f appears at the entrance of the feed side and then decreases along the flow direction until reaching a plateau when the flow is fully developed; while for the rest of the modules, the curves continuously decrease towards the exits. This is due to the slower build-up of the liquid boundary layer along the feed flow direction credited to the disturbance by the surface corrugations. Overall, the curves of modules with microstructured fibers are much higher than that of the original one, which shows the lowest average h_f of 1495 W m^{-2} K^{-1}. The configuration with an alternate wavy design 07 (1.25/1.0 mm, Lx = 1.25 m) shows the highest h_f of 6823.9 W m^{-2} K^{-1}, which is 4.6-fold higher than the original fiber, followed by another alternate wavy design 08 (2.5/1.0 mm, Lx = 2.5 m) and the gear-shaped fiber. The simulation results indicate that these new microstructured geometries have successfully introduced flow disturbance to disrupt the temperature polarization layer on the membrane surface and hence enhance the heat transfer. Also, the significant improvement of heat-transfer coefficients by introducing the corrugated surfaces has confirmed the controlling role of the liquid-boundary layers in this MD system with a large membrane coefficient C & low operating temperatures. More discussion of the flow-field distribution associated with intensified local mixing, reduced TP and enhanced permeation flux is presented in a later section.

In Fig. 4 (b) the curve of the heat-transfer coefficients on the permeate side h_p of the original module shows a similar trend to its h_f distribution − a continuous decrease appears after entering the inlet of the permeate side (L = 0.25 m) and then reaches a plateau. The modified designs wavy 01, 02, 03 and 06 follow the same trend. Surprisingly, wavy 02 (5.0/2.0 mm, b = 0.5) and 03 (5.0/2.0 mm, b = 0.8) even have lower h_p curves than the original fiber. The possible reason is that the presence of deeper waves (Δy = 2.0 mm) has created strong vortices in the valley zones on the permeate side, which caused liquid stagnation. However, the rest of the designs present an increasing h_p trend. It is observed that the gear-shaped design has the highest average h_p of a 5.5-fold increase compared to the original fiber, followed by a wavy geometry 05. For all the wavy configurations, the significant h_p enhancement is mainly due to the appropriate size of the corrugations that have greatly improved the hydrodynamic conditions and heat transfer at the permeate side, by increasing the surface shear-rate of the flow and hence reducing the thickness of liquid boundary layers; while for the gear-shaped design, the improved heat transfer at the permeate side was credited to the better hydrodynamic conditions on the corrugated outer membrane surface (i.e., feed side), which has much higher wall temperatures and hence a more efficient thermal diffusion across the thermal boundary layers at both sides.

It should be pointed out that different from the conclusions of our previous work on the introduction of external turbulence promoters into MD modules [42], the current h_p simulation results showed that microstructured designs on the membrane surface are able to improve the heat transfer not only at the feed but also at the permeate side.

3.1.2 Temperature-polarization mitigation and flow-filed visualization

It was observed in Fig. 4 that most of the modules with modified fiber geometries have shown significant enhancement in heat transfer coefficients h_f and h_p, which are closely related to the TP phenomenon—one of the critical barriers in MD practice. Thus, the corresponding results on TP effect are simulated and shown in Fig. 5, which gives the simulated *TPC* distributions along the module length L for all modules.

It can be seen from Fig. 5 that all modules present a similar U shape – the maximum *TPC* value occurs at the entrance and the lowest at the midpoint of the module then a slow increase towards the exit. The reason is that the transmembrane temperature difference ($T_{fm} - T_{pm}$) first decreases and then increases due to the opposite build-ups of thermal boundary layers on the feed and the permeate sides: the T_{fm} continues to decrease along its flow direction (x) and T_{pm} first increases and then decreases along $-x$ direction. It is not surprising to see that the modules with wavy designs 02 and 03 (5.0/2.0 mm, b = 0.5 and 0.8) show even lower *TPC* curves than the original straight one, which are consistent with those of the heat-transfer coefficients in Fig. 4, i.e., the continuous wavy designs 02 and 03 had lower h_p curves than the original straight fiber. The reason responsible for this result may be that a fiber surface with deep and over-frequent corrugations (waves) might result in intense local secondary flows, which are possibly trapped between the valleys of two neighboring projections and subsequently compromise the module performance. Hence, liquid stagnation would instead lead to a lower heat-transfer efficiency and more severe TP phenomenon.

On the other hand, the alternate wavy designs 07, 08 and gear structured modules present relatively higher *TPC* curves, which are also consistent with their high h_f and h_p distributions in Fig. 4. Compared to the original design, a *TPC* increase of 70 % is achieved by the gear-fiber module. This might be due to the intensified secondary flows induced by gear-shaped corrugations on the membrane surface that has reduced the thickness of thermal boundary layer and facilitated the heat transfer. For the alternate wavy designs 07 and 08, the reason for improvement may include two factors: firstly, these alternate wavy projections with an appropriate height have increased the surface roughness to create flow eddies and improve the hydrodynamic conditions on both sides; secondly, the presence of wavy corrugations have broadened the flow channel at the permeate side, which allows more cooling water to flow through and achieve better heat exchanging performance. Therefore, the temperature polarization phenomenon is greatly mitigated due to the effective flow alteration caused by modified flow channels. As a result, the overall driving force is increased.

To further reveal the fundamentals of the heat-transfer enhancement by employing microstructured fibers in MD modules, Fig. 6a shows the local flow-field and temperature distribution in modules with various fiber geometries (within a length range of 0.105−0.125 m with respect to the overall length 0.25 m). The velocity profiles are described by stream traces and temperature distribution in band colors. These simulation results are consistent with the trends of the heat-transfer coefficients curves shown in Fig. 4 and *TPC* distributions in Fig. 5 for these modified designs. Clearly, the intensity of secondary flows induced by the wavy corrugations increases with increasing wave depth and decreases with increasing the arching width. Nevertheless, it is shown that a microstructure of deeper and more frequent corrugations is not necessarily a superior choice for achieving improved module performance. For example, the wavy design 02 with continuous waves Δx of 2.5 mm and depth Δy of 2.0 mm showed a negative effect in terms of TP mitigation; while another lower wavy design 05 with continuous waves (Δx = 2.5 mm and Δy = 1.0 mm) performed much better. Interestingly, the alternative design 08 with less and low waves (Δx = 2.5 mm, Δy = 1.0 mm and Lx = 2.5 mm) achieved the best results among these three configurations. However, a further decrease in the number of turbulence aids might result in insufficient flow disturbance and mixing instead, which was reported in a prior study [42]. Due to the difficulty in presenting via a cross-sectional flow field, the flow conditions of the gear-fiber module is analyzed using the local temperature and pressure contours (slicing planes at x = 0.01, 0.10 and 0.20 m) in band colors, as shown in Fig. 6b. Compared to the module with an original straight fiber, the presence of a gear-shaped geometry successfully disrupts the liquid boundary layers on the feed side and simultaneously enhances the permeate flow. Hence, the TP effect is greatly reduced and heat transfer enhanced as indicated in Figs. 4 and 5. Thus, combining the simulation results shown in Figs. 4 and 5, it is concluded that an appropriate design of the membrane surface geometry can lead to reduced thermal boundary layers, alleviated TP phenomenon and hence enhanced heat transfer in a liquid-film controlled MD system.

3.1.3 Enhancement of permeation flux

Fig. 7 gives the distributions of mass fluxes N_m along the fiber length L for modules packed with fibers of various microstructural designs, under the same operating conditions. It is noted that N_m is defined based on the outer membrane area of the fiber. For the original module, the

N_m curve has a similar trend as its *TPC* distribution (shown in Fig. 5), which firstly decreased and then slightly increased due to the countercurrent build-ups of the thermal boundary layers on the feed and permeate sides. However, the modules with modified fibers show dramatic flux increase along the feed flow direction. This is due to the slower flow development and hence boundary layer buildup along a channel with corrugated surface.

Similar to the *TPC* results in Fig. 5, few configurations with modified fiber geometries show negative results compared to the original straight fiber — wavy 02, 03 and 04, which gain even lower average mass fluxes; while wavy 05 slightly outscores the original configuration. The highest flux enhancement of 60 % is achieved by the module with gear fibers, followed by the alternate wavy designs 07 and 08 with approximate improvement of 38 %. These modeling results again imply the advantages of a gear-shaped structure and alternate wavy geometries for achieving better module performance. However, the relatively lower fluxes per unit area of the continuous wavy designs 02−05 do not necessarily result in lower water production per day, due to the enhanced contact area generated by the corrugated geometry (a comparison of actual membrane areas A_s is given in Table 1). Therefore, a fair comparison will be provided in terms of water production (kg $\cdot$day^{-1}) in a later section.

3.2 Effect of fiber length for modules with various fiber geometric designs

Based on the previous discussions of the selected MD system (high *C* value and low operating temperatures), an appropriate modification of fiber geometry could greatly enhance the module performance. Thus, the most promising were selected to further explore their potential for industrial applications. A series of simulations were conducted to compare the length effect among single-fiber modules with original straight, wavy 08 and gear-shaped fibers. The results are shown in Figs. 8 and 9, which depict the effects of module length (L = 0.25, 0.54 and 0.84 m respectively) on the distributions of *TPC* and N_m along the dimensionless module length x/L under given operating conditions.

In Fig. 8 all *TPC* curves for different modules show U shapes with different curvatures. Regardless of fiber geometries, the average *TPC* values of these configurations decrease with increasing module length. i.e., shorter modules are less vulnerable to the TP effect and hence show higher *TPCs*. Overall, the modules with original straight fibers have the lowest curves among all configurations with the same lengths; while the ones with gear-shaped and wavy 08 fibers show similarly high *TPC*s. For the module with the original fiber, an increase of length from 0.25 m to 0.54 m causes 20 % *TPC* decrease; a further increase of length to 0.84 m results in an approximate 50 % decrease in the average *TPC*. Moreover, the shorter module (L = 0.25 m) presents a rather flat U shape compared to the longer ones with much slower flow development along the dimensionless length x/L. Yet, the module with a wavy design 08 presents 17 % decrease with a length increase from 0.25 m to 0.54 m and 21 % deterioration with a further increase to L = 0.84 m. The modules with gear-shaped fibers show a similar percentage of *TPC* decrease with increasing fiber length. Apparently, a much slower decrease with increasing fiber length is observed for modified fibers, due to a slower buildup of boundary layers at the same location (but a smaller x/L as the module gets longer). Although it was reported that longer modules tend to be subject to more severe TP effect [9], the simulated results in Fig. 8 show that fibers with modified geometries are advantageous for scale-up modules.

Fig. 9 shows the distributions of mass flux N_m for these three fiber geometries (straight, wavy 08 and gear-shaped) along the dimensionless module length x/L. In general, for the same configuration the local mass flux decreases with increasing module length at the same x/L, which is consistent with both our previous experimental data and simulation results [38, 44]. This is mainly due to the decrease in the local driving forces and the build-up of thermal boundary layers as the flow channel length increases. Except for a downward U shape for the module with a short straight fiber (0.25 m), the rest of the N_m curves show an upward U shape — a slight decrease at the entrance region, where the thinnest boundary layer of the feed side appears, and then an increase as the transmembrane temperature difference increases with increasing dimensionless length x/L. This is a result of the counter-current buildup of liquid boundary layers. Although longer modules with larger membrane areas will result in a higher water production, an optimized length should be chosen for industrial applications based on an acceptable magnitude of the local driving force and a more even distribution of N_m.

It is also observed in Fig. 9 that the N_m of the modified designs (wavy and gear-shaped) increases more significantly along the dimensionless module length x/L than the original module. This is mainly attributed to the increase of driving force as a result of disruptive boundary layers by surface corrugation. Overall, the modules with gear-shaped fibers gain the highest flux enhancement ratios among all configurations with the same length. Interestingly, compared to original modules, the gear-fiber configuration gains a slight increase of enhancement from 57 % to 65 % with increasing length from 0.25 m to 0.84 m. Therefore, it is meaningful to employ a modified fiber geometry like a gear-shaped, which performs more advantageously when longer modules are desired for a higher water production in industry.

3.3 Effects of flow conditions for modules with different fiber geometries

3.3.1 Reynolds number of the feed, Re_f

As a conventional strategy to improve hydrodynamic conditions in MD systems, an increase of flow velocity to create turbulence is found to be effective. However, similar to other hydrodynamic approaches [42], its effectiveness may differ in MD modules of different configurations. Based on the previous simulation results of geometric optimization, the gear-shaped design was selected and simulated to investigate the effect of flow conditions with modified surface geometry. With other operating conditions kept constant, Figs. 10 and 11 show the effects of flow conditions (in terms of Reynolds number, *Re*) on the *TPC* and mass flux N_m distributions for 0.25 m-long modules with single straight and gear fibers, respectively. In Fig. 10 (a) the average *TPC* increases with increasing Re_f for either configuration due to the improved fluid dynamics at a higher flow velocity. For the original module, all *TPC* distributions for varied feed flow conditions from laminar to turbulence (i.e., Re_f = 420 – 2500) show a similar U shape—initially decreasing after entering the module and then slowly increasing towards the exit; while the curves of the gear-fiber modules present a rather flat trend after leaving the entrance region. It is noted that the Re_f for the gear-fiber module was calculated based on the modified hydraulic diameter characterized by its gear-shaped surface.

Compared to the gear-fiber configuration, in Fig. 10 (a) the original module generally shows lower average *TPC* values and a negligible change with a velocity increase under laminar flow ($Re_f \leq 1500$). The *TPC* of the original module only fluctuates within 6 % with Re_f increasing from 420 to 1500; while the turbulence condition ($Re_f = 2500$) brings 30 % *TPC* increase compared to that of $Re_f = 420$. The dramatic enhancement is credited to the reduced thickness of liquid boundary layer and hence improved heat transfer under turbulent flow conditions. In contrast, the gear-fiber module shows fairly significant changes with the corresponding Re_f adjustment. This is probably because of the ups and downs of the gear-shaped surface, which could facilitate the occurrence of cross flow and hence enhanced fluid dynamics even at an extremely low Re_f. For instance, the gear-fiber module shows an encouraging average *TPC* of 0.7, which is 1.6 times higher than the original configuration, at the same low Re_f of 420.

In Fig. 10 (b) the mass flux N_m increases with increasing Re_f for both configurations. Similar to the *TPC* distributions, the N_m curves of the original module show a downward U shape along the fiber length *L* and have a rather insignificant response to a Re_f increase under laminar conditions ($Re_f \leq 1500$); its N_m distribution presents a dramatic increase along the feed flow direction once the turbulent condition is reached ($Re_f = 2500$). The maximum flux increase is up to 50 % compared to that of $Re_f = 420$. On the other hand, the gear-fiber module shows an initial decrease at the entrance and subsequent increase along the fiber length for each flow condition. Although a relatively flat curve is obtained at an extremely low Re_f of 420, the slope of the N_m curve for the gear-fiber configuration increases significantly with increasing Re_f. This indicates that the flow disturbance induced by the gear microstructure becomes more intense as the flow develops along the flow channel, especially at a higher flow velocity.

3.3.2 Reynolds number of the permeate, Re_p

Similarly, with the Re_f kept constant, the permeate flow conditions (Re_p) was varied to simulate the module performance in terms of TP alleviation and flux enhancement. Fig. 11 presents the *TPC* and N_m distributions along the fiber length *L* for both the original and gear-fiber modules with increasing Re_p from 220 to 2500. Similar to Fig. 10, the original module shows much lower *TPC* and N_m curves compared to the modified configuration at the same Re_p.

In Fig. 11 (a) the average *TPC* increases with increasing Re_p for both configurations. The reason is that a change in the heat-exchange rate at a higher Re_p leads to a decrease of permeate bulk temperature and hence a higher transmembrane temperature difference (driving force) occurs at the same fiber length. However, different from the influence of the feed flow conditions, a major increase of Re_p from laminar to turbulence only brings a modest change in their respective *TPC* results—an increase of 19 % occurs for the original module and 10 % for the gear-fiber one.

Similarly, Fig. 11(b) shows that the average N_m increases with increasing Re_p for both modules. Generally, at a relative higher Re_p ($\geq$ 1500) the N_m curves of both modules show an increasing trend along the permeate flow direction. This is because of a decrease of flow temperature on the permeate side, which results in an increasing transmembrane temperature difference towards the feed inlet (L = 0 m) at under-developed flow conditions. However, at an extremely low Re_p of 220 when the flow tends to be fully developed, the N_m curves of the original module shows a decreasing trend; while the gear-fiber module show a more dramatic decrease after the permeate flow enters the module. This is probably due to its particular corrugated gear structure that might regionally retain some liquid at low Re_p and hence result in a reduced local driving force due to a more rapid flow development and buildup of liquid boundary layer along the permeate flow direction. Nevertheless, compared to the original module, the gear-fiber module still gains 47 % flux enhancement at such a low Re_p of 220. Overall, a change in the flow conditions from laminar (Re_p = 220) to turbulence (Re_p = 2500) has brought significant influence on the permeation flux—32.5 % flux enhancement for the original module and 46 % for the gear-shaped fiber.

However, it should be pointed out that instead of employing high flow velocity to create turbulence, a major achievement of TP mitigation and flux enhancement could be accomplished by utilizing fibers with smarter microstructured designs under laminar conditions.

3.4 Comparison of water production and hydraulic loss for modules with various fiber geometries

As discussed in the previous sections, an appropriate geometric modification on the membrane surface (e.g., alternate wavy or geared shapes) would greatly reduce the heat-transfer resistance and improve the module performance, when the heat transferred through the liquid-boundary layers presents a dominant resistance. To fully evaluate these fibers of various geometries, two important process metrics—water production (kg day^{-1}) and hydraulic energy consumption (*HEC*) were calculated and compared among various modules (geometric specifications listed in Table 1), as shown in Fig. 12. Assuming that each ideal module contains one-hundred pieces of fiber with different geometric designs (i.e., total membrane area $A = 100\ A_s$), the configuration with original straight fibers has a *HEC* of 6.5 J kg^{-1} and water production of 46 kg day^{-1}; while the module with gear fibers shows the highest water production of 136 kg day^{-1} but the lowest *HEC* of 3.5 J kg^{-1}, followed by the alternate wavy designs 01, 07 and 08. Although the continuous wavy designs 02 and 03 also gain reasonably high water production, they tend to be subject to high hydraulic loss (> 20 J·kg^{-1}). Overall, the gear-fiber module shows the most promising features for achieving approximately 3-fold water production enhancement with only half of the hydraulic loss, compared to the original design.

4. Conclusions

In this study a series of CFD simulations were carried out to explore the potential benefits of employing microstructured hollow fiber membranes used in a DCMD system.

It is found that the module with fibers of gear-shaped structure acheives the highest average *TPC* and mass flux N_m values compared to the original straight design, followed by the alternate wavy fibers. The enhanced performance of modified modules can be attributed to the improved hydrodynamics caused by intense secondary flows and improved surface renewal with the presence of corrugations on the membrane surface, which is confirmed by the observation of the flow-field and temperature profiles from the CFD simulations. The investigations on fiber-length effect show that the gear-shaped fiber modules provide the highest flux enhancement ratios with equivalent effective lengths, followed by the modules with alternate wavy fibers. Interestingly, the advantages of the smart fiber designs are further amplified for longer modules, which is attractive for scale-up to a higher total water production in industrial applications.

Investigations of the flow conditions showed that the gear- shaped fiber module has a promising enhancement at an extremely low *Re*. Although a flow transition from laminar to turbulent conditions would bring a significant improvement in a conventional MD module, introducing a smart microstructured design into the membrane surface would be a cost-effective option under adverse flow conditions. Also, the computed water production and hydraulic energy consumption (*HEC*) of different modules with various fiber geometries have been compared. The configuration with gear-shaped fibers has the highest water production but the lowest *HEC*. In addition, a high water production can be obtained using modules with wavy fibers, due to their greatly increased membrane area by surface corrugations. However, these geometries might possibly cause higher *HEC*. It is hoped that this study can bring a new perspective on the development of smart membranes for MD applications, and provide a foundation to guide the fabrication of microstructured hollow fiber membranes with an optimal design.

Acknowledgments

Support from Siemens Water Technology is gratefully acknowledged. The authors also thank the Singapore Economic Development Board (**EDB**) for funding the Singapore Membrane Technology Centre (SMTC) where this study was performed.

Nomenclatures

A	total membrane area of 100 fibers (m^2)
A_s	membrane area of a single fiber (m^2)
b	shape parameter of the wavy arch on the membrane surface
C	membrane distillation coefficient of the membrane (kg m^{-2} s^{-1} Pa^{-1})
c_p	specific heat capacity of material (J kg^{-1} K^{-1})
d_i	inner diameter of the hollow fiber (mm)
d_o	outer diameter of the hollow fiber (mm)
h	local heat-transfer coefficient of fluids and membrane (W m^{-2} K^{-1})
ΔH_T	latent heat of vaporization of water at temperature T (J kg^{-1})
k	thermal conductivity (W m^{-1} K^{-1})
L_b	dimension of a gear with a square shape (mm)
Lx	interval between two corrugated waves on the membrane surface (mm)
N_m	transmembrane mass flux (kg m^{-2} s^{-1})
P	water vapor pressure (Pa)
ΔP_{fluid}	pressure drop along the module length in the shell side (Pa)
Q	heat-transfer rate through the liquid film (W)
q	heat flux (W m^{-2})
q_{MD}	transmembrane latent heat flux (W m^{-2})
q_{HL}	conductive heat loss (W m^{-2})
Re	Reynolds number
R_{mi}, R_{mo}	inner, outer radii of hollow fiber (m)
S_h	source term of energy transport equation (J m^{-3} s^{-1}), $S_h = \begin{cases} \frac{q_{MD}}{\delta r} \cdot \frac{R_{mo}}{R_{mi}} & \text{for } r = R_{mi} \\ -\frac{q_{MD}}{\delta r} & \text{for } r = R_{mo} \\ 0 & \text{otherwise} \end{cases}$
T	temperature (K)
v	velocity of feed or permeate (m s^{-1})
V	volumetric flow rate of the fluid (m^3 s^{-1})

u	normalized velocity of feed or permeate (m s^{-1})
x, r	axial, radial directions in cylindrical coordinate (m)
Δx	cross-sectional dimension of the wavy arch in x direction (mm)
Δy	cross-sectional dimension of the wavy arch in r direction (mm)

Greek letters

α	interval angle between two neighboring gears on the cross section of the fiber
$\bar{\bar{\tau}}$	stress tensor (kg m^{-1} s^{-1}) $\bar{\bar{\tau}} = \mu \left[\left(\nabla \vec{v} + \nabla \vec{v}^{T} \right) - \frac{2}{3} \nabla \cdot \vec{v} I \right]$
μ	viscosity (Pa s)
ρ	Density (kg m^{-3})
δ_m	membrane wall thickness (mm)
δ_r	grid scale in the r direction

Suffix

b	bulk average
f	Feed
fm	feed-side membrane surface
m	membrane, or membrane surface
i, o	inlet and outlet of fluids
p	Permeate
pm	permeate-side membrane surface
HL	Heat loss

References

[1] M. S. El-Bourawi, Z. Ding, R. Ma and M. Khayet, A framework for better understanding membrane distillation separation process, Journal of Membrane Science, 285 (1-2) (2006) 4-29

[2] H. Susanto, Towards practical implementations of membrane distillation, Chem. Eng. Process., 50 (2011) 139-150

[3] R. W. Schofield, A. G. Fane and C. J. Fell, Heat and mass transfer in membrane distillation, J. Membr. Sci., (33) (1987) 299-313

[4] K. W. Lawson and D. R. Lloyd, Membrane distillation, J. Membr. Sci., 124 (1) (1997) 1-25

[5] M. Khayet, Membranes and theoretical modeling of membrane distillation: a review, Adv. Colloid Interface Sci., In Press (2011)

[6] A. Chanachai, K. Meksup and R. Jiraratananon, Coating of hydrophobic hollow fiber PVDF membrane with chitosan for protection against wetting and flavor loss in osmotic distillation process, Separation and Purification Technology, 72 (2) (2010) 217-224

[7] M. Su, M. M. Teoh, K. Y. Wang, J. Su and T.-S. Chung, Effect of inner-layer thermal conductivity on flux enhancement of dual-layer hollow fiber membranes in direct contact membrane distillation, J. Membr. Sci., 364 (1-2) (2010) 278-289

[8] J. Zhang, J.-D. Li, M. Duke, Z. Xie and S. Gray, Performance of asymmetric hollow fibre membranes in membrane distillation under various configurations and vacuum enhancement, J. Membr. Sci., 362 (1-2) (2010) 517-528

[9] X. Yang, R. Wang, L. Shi, A. G. Fane and M. Debowski, Performance improvement of PVDF hollow fiber-based membrane distillation process, J. Membr. Sci., 369 (1-2) (2011) 437-447

[10] L. Song, B. Li, K. Sirkar and J. Gilron, Direct contact membrane distillation-based desalination: novel membranes, devices, larger-scale studies, and a model, Ind. Eng. Chem. Res., 46 (8) (2007) 2307-2323

[11] P. Wang, M. M. Teoh and T.-S. Chung, Morphological architecture of dual-layer hollow fiber for membrane distillation with higher desalination performance, Water Research, 45 (17) (2011) 5489-5500

[12] M. Khayet, T. Matsuura and J. I. Mengual, Porous hydrophobic/hydrophilic composite membranes: estimation of the hydrophobic layer thickness, J. Membr. Sci., 266 (2005) 68-79

[13] B. Li and K. K. Sirkar, Novel membrane and device for vacuum membrane distillation-based desalination process, J. Membr. Sci., 257 (1-2) (2005) 60-75

[14]M. Khayet, T. Matsuura, J. I. Mengual and M. Qtaishat, Design of novel direct contact membrane distillation membranes, Desalination, 192 (1-3) (2006) 105-111

[15]M. Qtaishat, D. Rana, M. Khayet and T. Matsuura, Preparation and characterization of novel hydrophobic/hydrophilic polyetherimide composite membranes for desalination by direct contact membrane distillation, J. Membr. Sci., 327 (1-2) (2009) 264-273

[16]B. Li and K. K. Sirkar, Novel Membrane and Device for Direct Contact Membrane Distillation-Based Desalination Process, Ind. Eng. Chem. Res., 43 (17) (2004) 5300-5309

[17]T. Y. Cath, V. D. Adams and A. E. Childress, Experimental study of desalination using direct contact membrane distillation: a new approach to flux enhancement, J. Membr. Sci., 228 (1) (2004) 5-16

[18]L. Martinez and J. M. Rodriquez-Maroto, Effects of membrane and module design improvements on flux in direct contact membrane distillation, Desalination, 205 (1-3) (2007) 97-103

[19]M. M. Teoh, S. Bonyadi and T.-S. Chung, Investigation of different hollow fiber module designs for flux enhancement in the membrane distillation process, J. Membr. Sci., 311 (1-2) (2008) 371-379

[20]K. W. Lawson and D. R. Lloyd, Membrane distillation. II. Direct contact MD, J. Membr. Sci., 120 (1) (1996) 123-133

[21]R. W. Schofield, A. G. Fane and C. J. D. Fell, The efficient use of energy in membrane distillation, Desalination, 64 (1987) 231-243

[22]L. Martinez-Diez and M. I. Vazquez-Gonzalez, A method to evaluate coefficients affecting flux in membrane distillation, J. Membr. Sci., 173 (2) (2000) 225-234

[23]M. Qtaishat, T. Matsuura, B. Kruczek and M. Khayet, Heat and mass transfer analysis in direct contact membrane distillation, Desalination, 219 (1-3) (2008) 272-292

[24]L. Martinez and J. M. Rodriquez-Maroto, Characterization of membrane distillation modules and analysis of mass flux enhancement by channel spacers, J. Membr. Sci., 274 (1-2) (2006) 123-137

[25]J. Phattaranawik, R. Jiraratananon, A. G. Fane and C. Halim, Mass flux enhancement using spacer filled channels in direct contact membrane distillation, J. Membr. Sci., 187 (1-2) (2001) 193-201

[26]Z. Ding, L. Liu and R. Ma, Study on the effect of flow maldistribution on the performance of the hollow fiber modules used in membrane distillation, J. Membr. Sci., 215 (2003) 11-23

[27]L. Cheng, P. Wu and J. Chen, Modeling and optimization of hollow fiber DCMD module for desalination, J. Membr. Sci., (318) (2008) 154–166

[28] R. Schneider, W. Hölz, R. Wollbeck and S. Ripperger, Membranes and modules for transmembrane distillation, J. Membr. Sci., 39 (1) (1988) 25-42

[29] X. Yang, R. Wang and A. G. Fane, Novel designs for improving the performance of hollow fiber membrane distillation modules, J. Membr. Sci., 384 (1-2) (2011) 52-62

[30] C.J.M. van Rijn, L. Vogelaar, W. Nijdam, J.N. Barsema and M.Wessling, Method of making a product with a micro or nano sized structure and product, WO Patent 0,243,937 (2002)

[31] A. Herczeg, Convoluted surface hollow fiber membranes, US Patent 6,805,730 (2004)

[32] W. Nijdam, J. d. Jong, C. J. M. v. Rijn, T. Visser, L. Versteeg, G. Kapantaidakis, G.-H. Koops and M. Wessling, High performance micro-engineered hollow fiber membranes by smart spinneret design, J. Membr. Sci., (256) (2005) 209-215

[33] P. Z. Çulfaza, E. Rolevink, C. v. Rijn, R. G. H. Lammertink and M. Wessling, Microstructured hollow fibers for ultrafiltration, J. Membr. Sci., (347) (2010) 32-41

[34] P. Z. Çulfaza, M. Wessling and R. G. H. Lammertink, Fouling behavior of microstructured hollow fiber membranes in submerged and aerated filtrations, Water Research, (45) (2011) 1865-1871

[35] P. Z. Çulfaza, M. Haddad, M. Wessling and R. G. H. Lammertink, Fouling behavior of microstructured hollow fibers in cross-flow filtrations: Critical flux determination and direct visual observation of particle deposition, J. Membr. Sci., 372 (2011) 210-218

[36] M. Hashino, T. Katagiri, N. Kubota, Y. Ohmukai, T. Maruyama and H. Matsuyama, Effect of surface roughness of hollow fiber membranes with gear-shaped structure on membrane fouling by sodium alginate, J. Membr. Sci., (366) (2011) 389–397

[37] G. A. Fimbres-Weihs and D. E. Wiley, Review of 3D CFD modeling of flow and mass transfer in narrow spacer-filled channels in membrane modules, Chem. Eng. Process., 49 (7) (2010) 759-781

[38] H. Yu, X. Yang, R. Wang and A. G. Fane, Numerical simulation of heat and mass transfer in direct membrane distillation in a hollow fiber module with laminar flow, J. Membr. Sci., 384 (1-2) (2011) 107-116

[39] H. J. Hwang, K. He, S. Gray, J. Zhang and I. S. Moon, Direct contact membrane distillation (DCMD): Experimental study on the commercial PTFE membrane and modeling, J. Membr. Sci., 371 (1-2) 90-98

[40] M. Shakaib, S. M. F. Hasani, I. Ahmed and R. M. Yunus, A CFD study on the effect of spacer orientation on temperature polarization in membrane distillation modules, Desalination, 284 (2012) 332-340

[41] H. Yu, X. Yang, R. Wang and A. G. Fane, Analysis of heat and mass transfer by CFD for

performance enhancement in direct contact membrane distillation, J. Membr. Sci., 405- 406 (2012) 38- 47

[42] X. Yang, H. Yu, R. Wang and A. G. Fane, Analysis on the effect of turbulence promoters in hollow fiber membrane distillation module via computational fluid dynamic (CFD) simulations, J. Membr. Sci., submitted (2012)

[43] R. W. Schofield, A. G. Fane, C. J. D. Fell and R. Macoun, Factors affecting flux in membrane distillation, Desalination, 77 (1990) 279-294

[44] X. Yang, R. Wang, L. Shi, A. G. Fane and M. Debowski, Performance improvement of PVDF hollow fiber-based membrane distillation process, Journal of Membrane Science, (2010), doi:10.1016/j.memsci.2010.12.020

List of Figures

Fig. 1. (a) Schematic of axially-symmetry single fiber modules in CFD simulating domains; (b) local domain amplification of an axially-symmetry wavy single-fiber module in CFD simulations

Fig. 2. 3D geometric structures of modules with (a) wavy fiber; (b) gear-shaped fiber

Fig. 3. Local mesh schemes of a module with the original straight fiber

Fig. 4. h_f & h_p distributions along the fiber length for single-fiber modules with fiber of various geometries (C = 8.0×10^{-7} kg m^{-2} s^{-1} Pa^{-1} and C^*(gear) = 6.4×10^{-7} kg m^{-2} s^{-1} Pa^{-}1, L = 0.25m, T_{fi} = 327.15 K, T_{pi} = 293.85 K, u_{fi} = 0.06 m s^{-1}, u_{pi} = 0.417 m s^{-1})

Fig. 5. *TPC* distributions along the fiber length for single-fiber modules with fiber of various geometries (C = 8.0×10^{-7} kg m^{-2} s^{-1} Pa^{-1} and C^*(gear) = 6.4×10^{-7} kg m^{-2} s^{-1} Pa^{-}1, L = 0.25 m, T_{fi} = 327.15 K, T_{pi} = 293.85 K, u_{fi} = 0.06 m s^{-1}, u_{pi} = 0.417 m s^{-1})

Fig. 6. (a) Local flow-field visualization for modules with fibers of various wavy designs; (b) Comparison of local temperature and pressure distributions for single-fiber modules with (i) originalstraight fiber; (ii) gear fiber (C = 8.0×10^{-7} kg m^{-2} s^{-1} Pa^{-1} and C^*(gear) = 6.4×10^{-7} kg m^{-2} s^{-1} Pa^{-}1, L = 0.25 m, T_{fi} = 327.15 K, T_{pi} = 293.85 K, u_{fi} = 0.06 m s^{-1}, u_{pi} = 0.417 m s^{-1})

Fig. 7. Mass flux N_m distribution along the fiber length for single-fiber modules with fiber of various geometries (C = 8.0×10^{-7} kg m^{-2} s^{-1} Pa^{-1} and C^*(gear) = 6.4×10^{-7} kg m^{-2} s^{-1} Pa^{-}1, L = 0.25m, T_{fi} = 327.15 K, T_{pi} = 293.85 K, u_{fi} = 0.06 m s^{-1}, u_{pi} = 0.417 m s^{-1})

Fig. 8. Effect of fiber length I: *TPC* distributions for single-fiber modules with fiber of various geometries (C = 8.0×10^{-7} kg m^{-2} s^{-1} Pa^{-1} and C^*(gear) = 6.4×10^{-7} kg m^{-2} s^{-1} Pa^{-}1, L = 0.25, m 0.54 and 0.84 m, T_{fi} = 327.15 K, T_{pi} = 293.85 K, u_{fi} = 0.06 m s^{-1}, u_{pi} = 0.417 m s^{-1})

Fig. 9. Effect of fiber length II: mass flux N_m distributions for single-fiber modules with fiber of various geometries (C = 8.0×10^{-7} kg m^{-2} s^{-1} Pa^{-1} and C^*(gear) = 6.4×10^{-7} kg m^{-2} s^{-1} Pa^{-}1, L = 0.25, 0.54 and 0.84 m, T_{fi} = 327.15 K, T_{pi} = 293.85 K, u_{fi} = 0.06 m s^{-1}, u_{pi} = 0.417 m s^{-1})

Fig. 10. Effect of feed flow conditions (Re_f) for fibers of single-fiber modules with original straight and gear-shaped fibers (a) TPC distributions; (b) N_m distributions (C = 8.0×10^{-7} kg m^{-2} s^{-1} Pa^{-1} and C^*(gear) = 6.4×10^{-7} kg m^{-2} s^{-1} Pa^{-}1, L = 0.25 m, T_{fi} = 327.15 K, T_{pi} = 293.85 K, Re_f = 420–2500, Re_p = 460)

Fig. 11. Effect of permeate flow conditions (Re_p) for fibers of original straight and gear-shaped fibers (C = 8.0×10^{-7} kg m^{-2} s^{-1} Pa^{-1} and C^*(gear) = 6.4×10^{-7} kg m^{-2} s^{-1} Pa^{-}1, L = 0.25 m, T_{fi} = 327.15 K, T_{pi} = 293.85 K, Re_f = 836, Re_p = 220–2500)

Fig. 12. Comparison of water production in multi-fiber modules with various fiber geometries (each module contains100 fibers, $A = 100A_s$, C = 8.0×10^{-7} kg m^{-2} s^{-1} Pa^{-1} and C^*(gear) = 6.4×10^{-7} kg m^{-2} s^{-1} Pa^{-}1, L = 0.25 m, u_{fi} = 0.06 m s^{-1}, u_{pi} = 0.417 m s^{-1}, T_{fi} = 327.15 K, T_{pi} = 293.85 K)

List of Tables

Table 1. Specification of various fiber geometric designs

Table. 2. Summary of CFD mathematical models, boundary conditions and algorithms

Table. 3. Summary of heat-transfer equations and definitions in MD

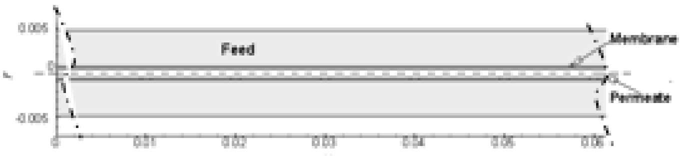

(i)Original module

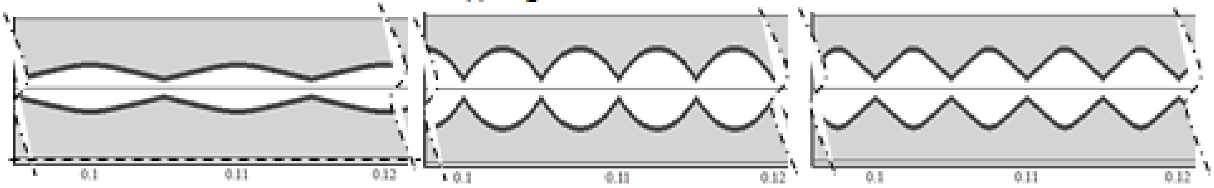

(ii) Wavy 01, 5.0/1.0, b=0.8 (iii) Wavy 02, 2.5/ 2.0, b=0.5 (iv) wavy03, 2.5/2.0, b=0.8

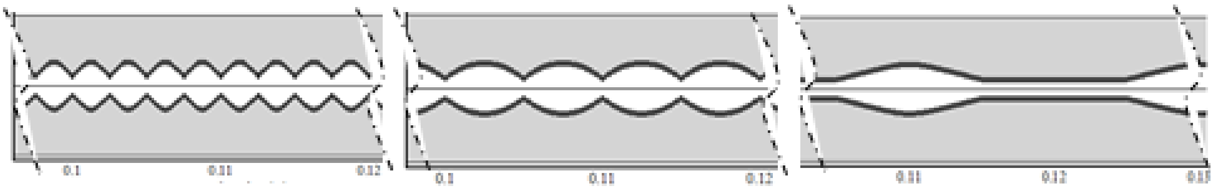

(v) wavy04, 1.25/1.0 , b=0.7 (vi) wavy05, 2.5/ 1.0, b=0.5 (vii) wavy06, alternate 5.0/1.0, b=0.8

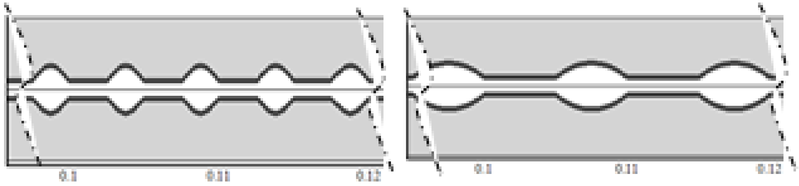

(viii) wavy07, alternate, 1.25/1.0 , b=0.7 (ix) wavy08, alternate 2.5/ 1.0, b=0.5

Fig. 1a. Schematic of axially-symmetry single fiber modules in CFD simulating domains

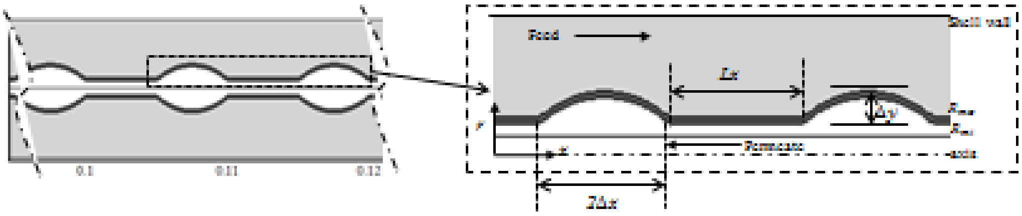

Fig. 1b. local domain amplification of an axially-symmetry wavy single-fiber module in CFD simulations

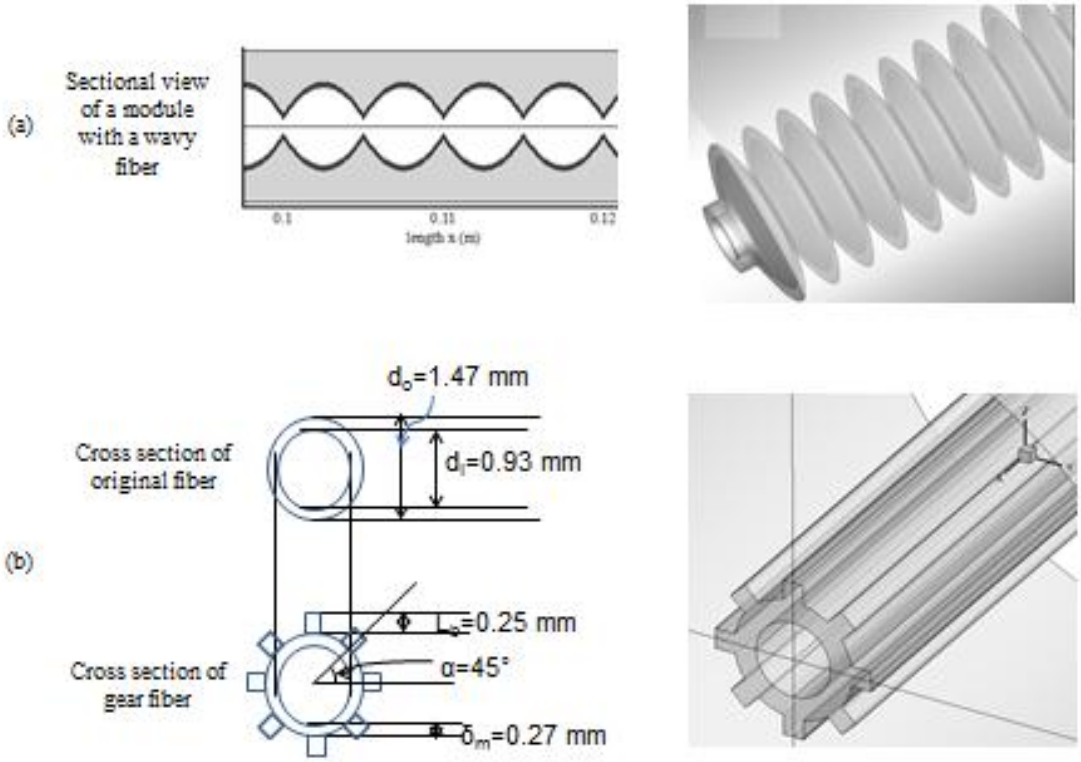

Fig. 2. 3D geometric structures of modules with (a) wavy fiber; (b) gear-shaped fiber

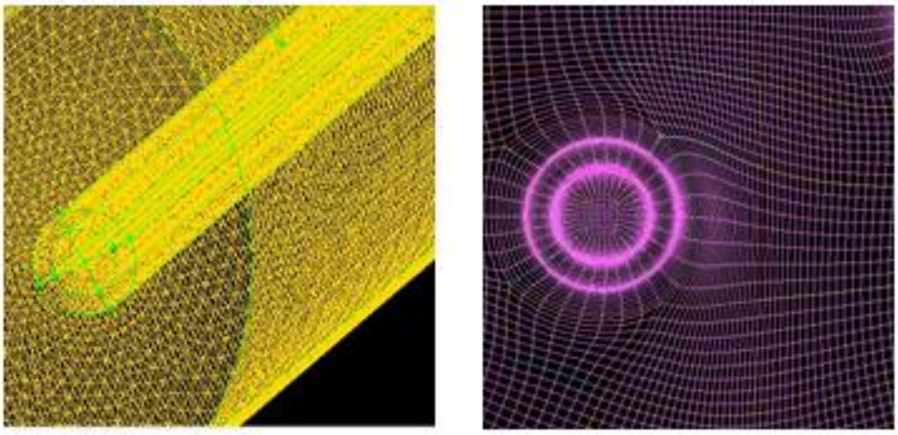

Fig. 3. Local mesh schemes of the 3D structure for a module with the original straight fiber

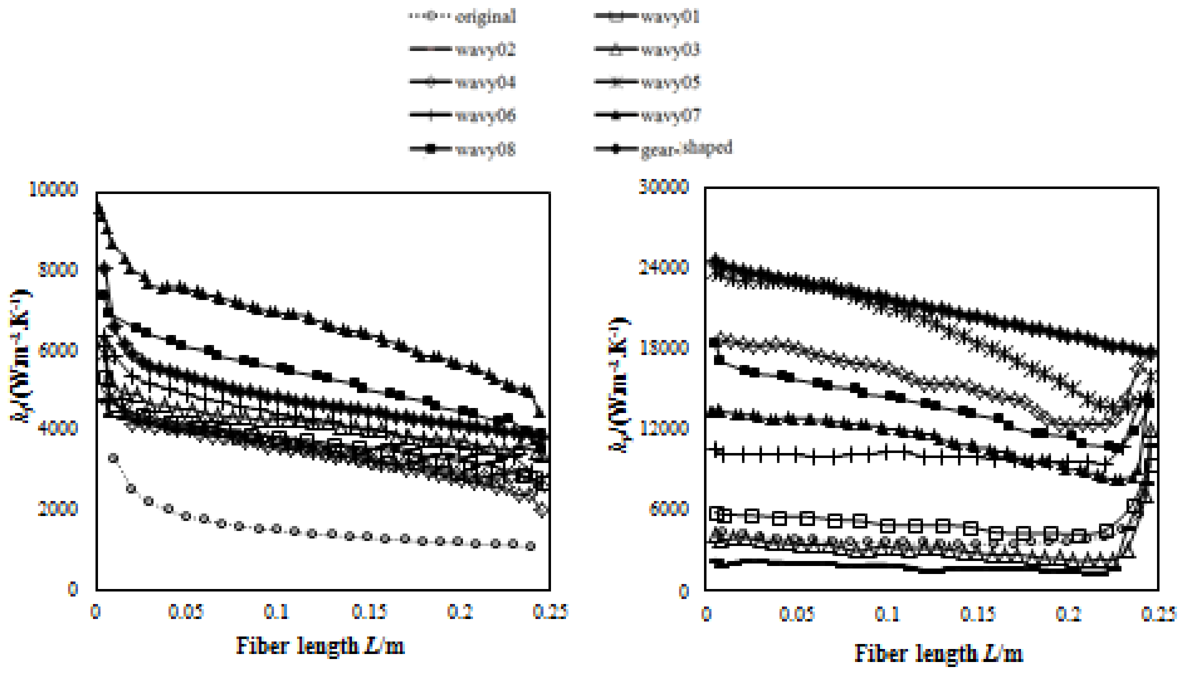

(a) h_f distributions vs. module length *L*

(b) h_p distributions vs. module length *L*

Fig. 4. h_f & h_p distributions along the fiber length for single-fiber modules with fiber of various geometries ($C = 8.0\times10^{-7}$ kg·m^{-2}·s^{-1}·Pa^{-1} and C^*(gear) $= 6.4\times10^{-7}$ kg·m^{-2}·s^{-1}·Pa^{-1} , $L = 0.25$ m, $T_{fi} = 327.15$ K, $T_{pi} = 293.85$ K, $u_{fi} = 0.06$ m·s^{-1}, $u_{pi} = 0.417$ m·s^{-1})

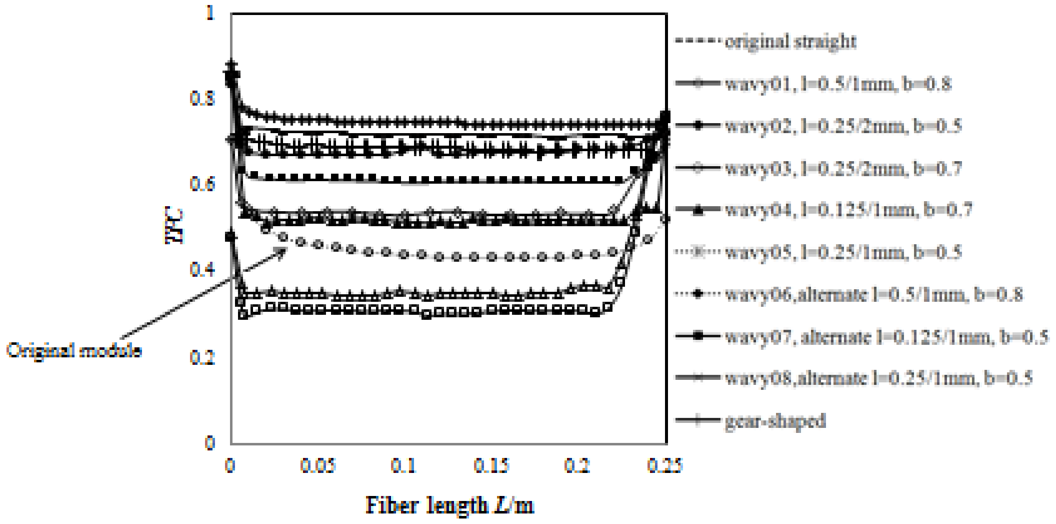

Fig. 5. *TPC* distributions along the fiber length for single-fiber modules with fiber of various geometries ($C = 8.0\times10^{-7}$ kg·m^{-2}·s^{-1}·Pa^{-1} and C^*(gear) $= 6.4\times10^{-7}$ kg·m^{-2}·s^{-1}·Pa^{-1}, $T_{fi} = 327.15$ K, $T_{pi} = 293.85$ K, $L = 0.25$ m, $u_{fi} = 0.06$ m·s^{-1}, $u_{pi} = 0.417$ m·s^{-1})

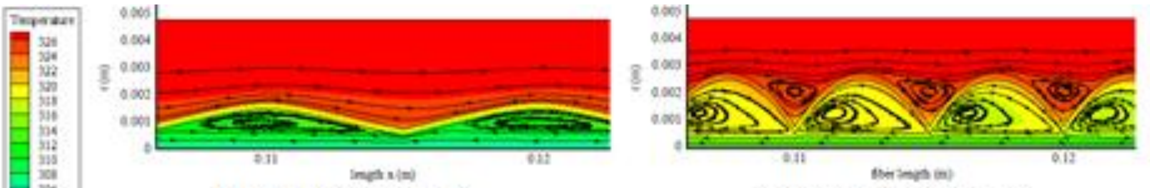

(b) Wavy 01, 5.0/1.0, b=0.8

(c) Wavy 02, 2.5/ 2.0, b=0.5

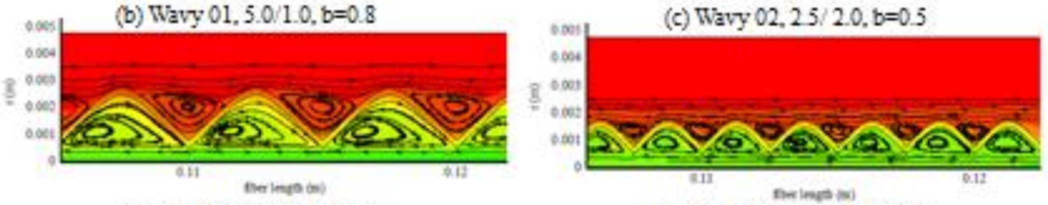

(d) wavy03, 2.5/2.0, b=0.8

(e) wavy04, 1.25/1.0 , b=0.7

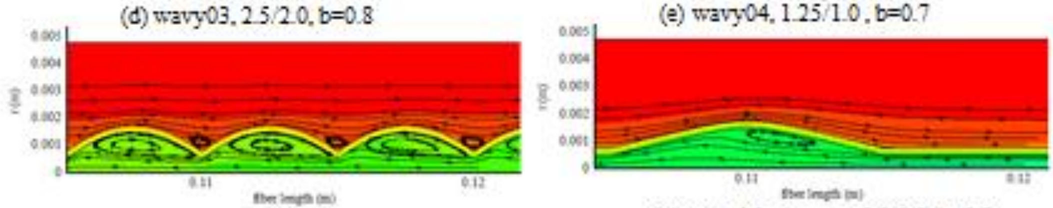

(f) wavy05, 2.5/ 1.0, b=0.5

(g) wavy06, alternate 5.0/1.0, b=0.8

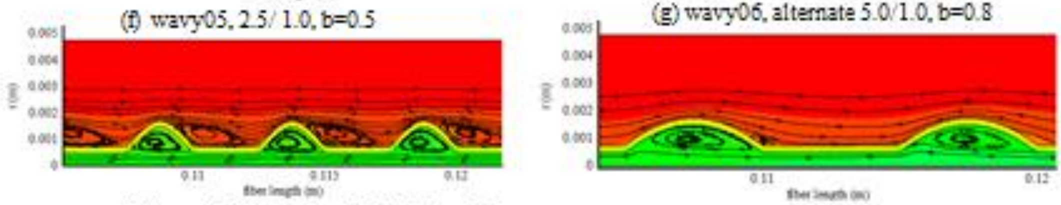

(h) wavy07, alternate, 1.25/1.0 , b=0.7

(i) wavy08, alternate 2.5/ 1.0, b=0.5

Fig. 6a. Local flow field visualization for modules with fibers of various wavy designs ($C = 8.0\times10^{-7}$ kg·m^{-2}·s^{-1}·Pa^{-1}, $L = 0.25$ m, $T_{fi} = 327.15$ K, $T_{pi} = 293.85$ K, $u_{fi} = 0.06$ m·s^{-1}, $u_{pi} = 0.417$ m·s^{-1})

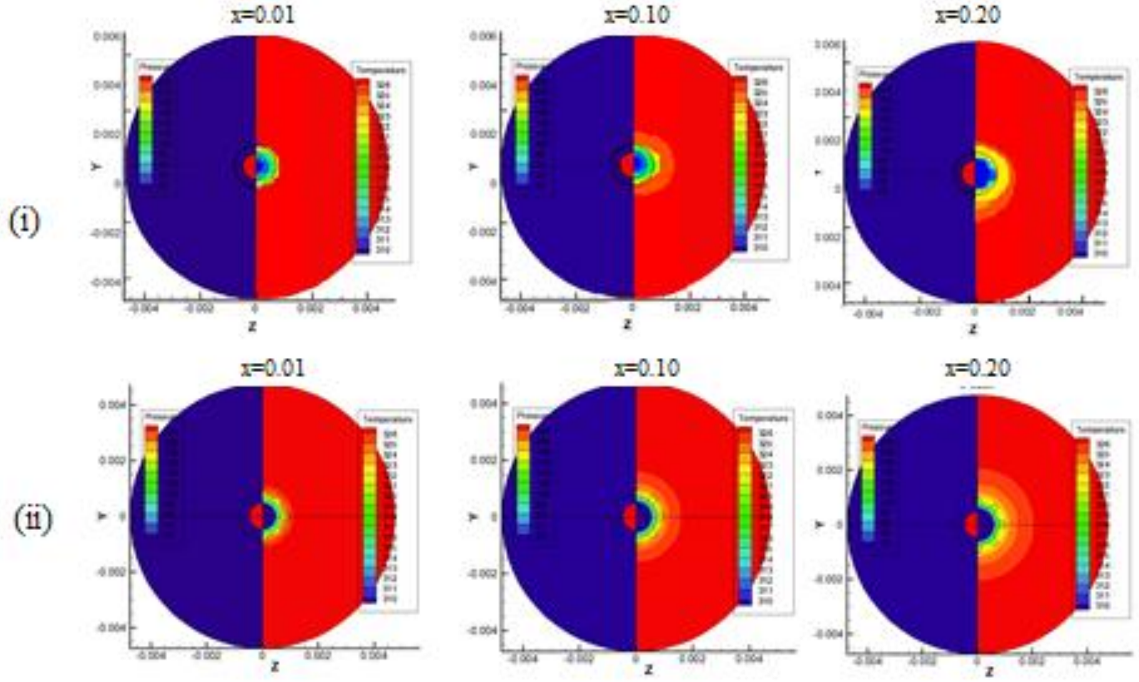

Fig. 6b. Comparison of local temperature and pressure distributions for single-fiber modules with (i) original straight fiber; (ii) gear fiber ($C = 8.0\times10^{-7}$ kg·m^{-2}·s^{-1}·Pa^{-1} and C*(gear) = 6.4×10^{-7} kg·m^{-2}·s^{-1}·Pa^{-1}, $L = 0.25$ m, $T_{fi} = 327.15$K, $T_{pi} =$ 293.85K, $u_{fi} = 0.06$m·s^{-1}, $u_{pi} = 0.417$ m·s^{-1})

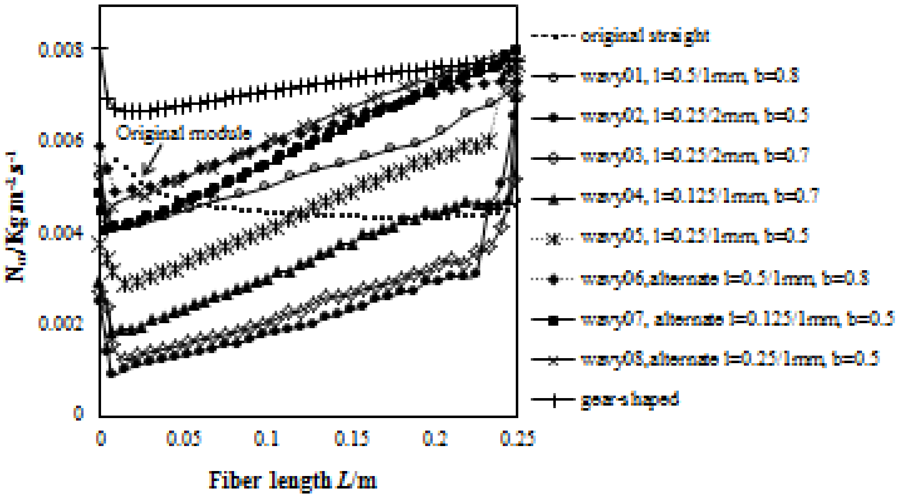

Fig. 7. Mass flux N_m distributions along the fiber length for single-fiber modules with fiber of various geometries ($C = 8.0 \times 10^{-7}$ kg·m^{-2}·s^{-1}·Pa^{-1} and C^*(gear) = 6.4×10^{-7} kg·m^{-2}·s^{-1}·Pa^{-1}, L=0.25, 0.54 and 0.84 m, T_{fi} = 327.15 K, T_{pi} = 293.85 K, u_{fi} = 0.06 m·s^{-1}, u_{pi} = 0.417 m·s^{-1})

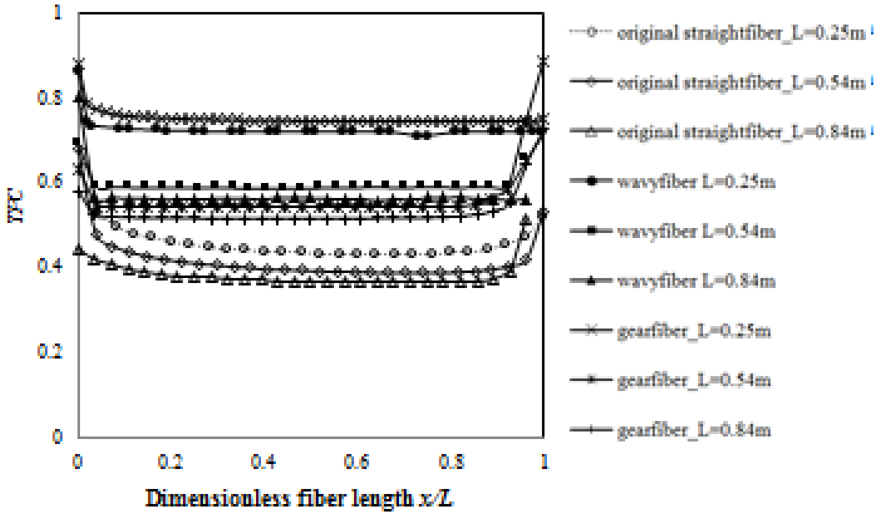

Fig. 8. Effect of fiber length I: *TPC* distributions for single-fiber modules with fiber of various geometries
($C = 8.0 \times 10^{-7}$ kg·m^{-2}·s^{-1}·Pa^{-1} and C^*(gear) = 6.4×10^{-7} kg·m^{-2}·s^{-1}·Pa^{-1}, L = 0.25, 0.54 and 0.84 m, T_{fi} = 327.15 K, T_{pi} = 293.85 K, u_{fi} = 0.06 m·s^{-1}, u_{pi} = 0.417 m·s^{-1})

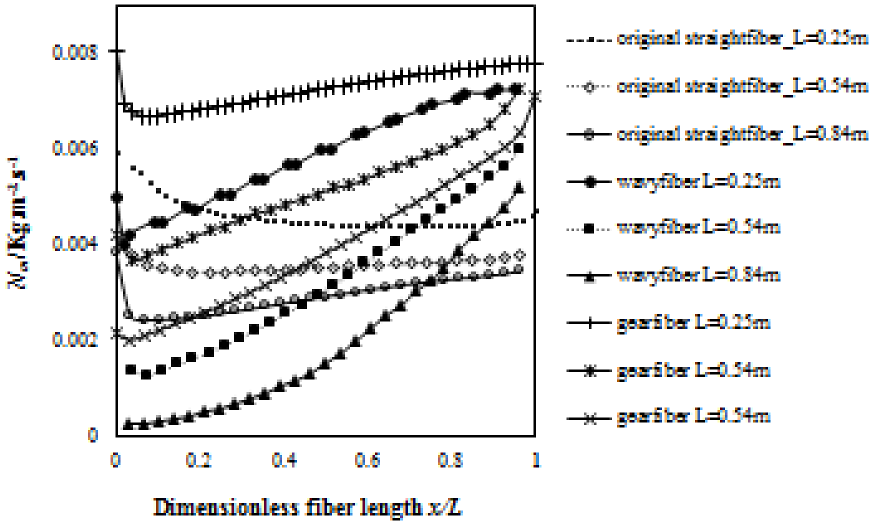

Fig. 9. Effect of fiber length II: mass flux N_m distributions for single-fiber modules with fiber of various geometries
($C = 8.0\times10^{-7}$ kg·m^{-2}·s^{-1}·Pa^{-1} and C*(gear)= 6.4×10^{-7} kg·m^{-2}·s^{-1}·Pa^{-1}, $L = 0.25$ m, $T_{fi} = 327.15$K, $T_{pi} = 293.85$K, $u_{fi} = 0.06$ m·s^{-1}, $u_{pi} = 0.417$ m·s^{-1})

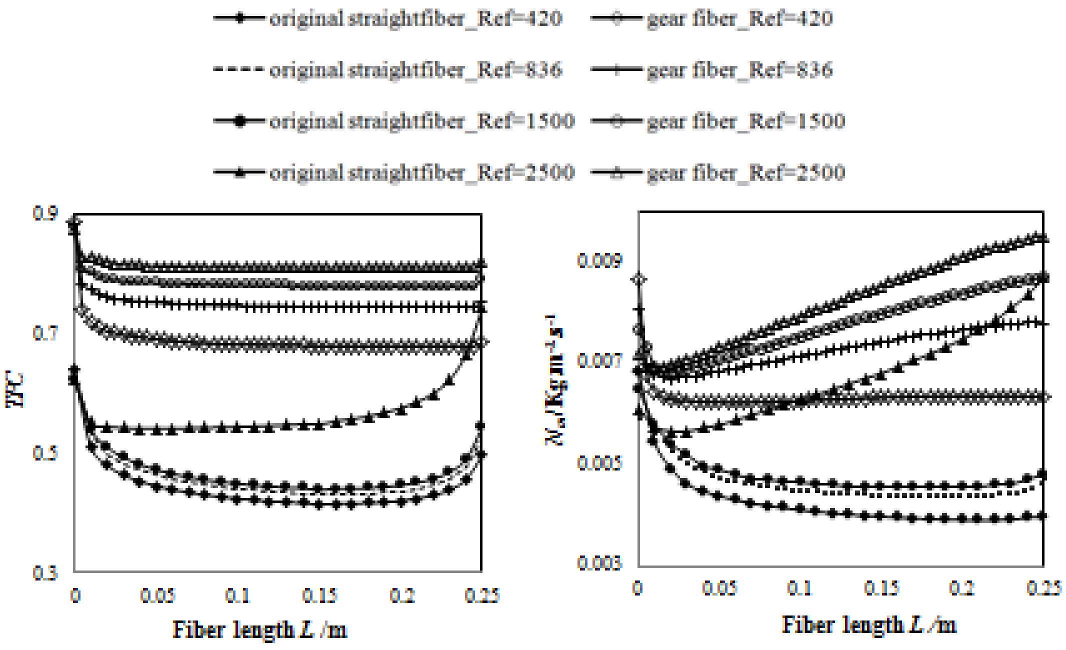

(a) *TPC* distributions

(b) N_m distributions

Fig. 10. Effect of feed flow conditions (Re_f) for fibers of single-fiber modules with original straight and gear-shaped fibers (a) *TPC* distributions; (b) N_m distributions
($C = 8.0\times10^{-7}$ kg·m^{-2}·s^{-1}·Pa^{-1} and C*(gear)= 6.4×10^{-7} kg·m^{-2}·s^{-1}·Pa^{-1}, $L = 0.25$ m, $T_{fi} = 327.15$K, $T_{pi} = 293.85$K, $Re_f = 420$–2500, $Re_p = 460$)

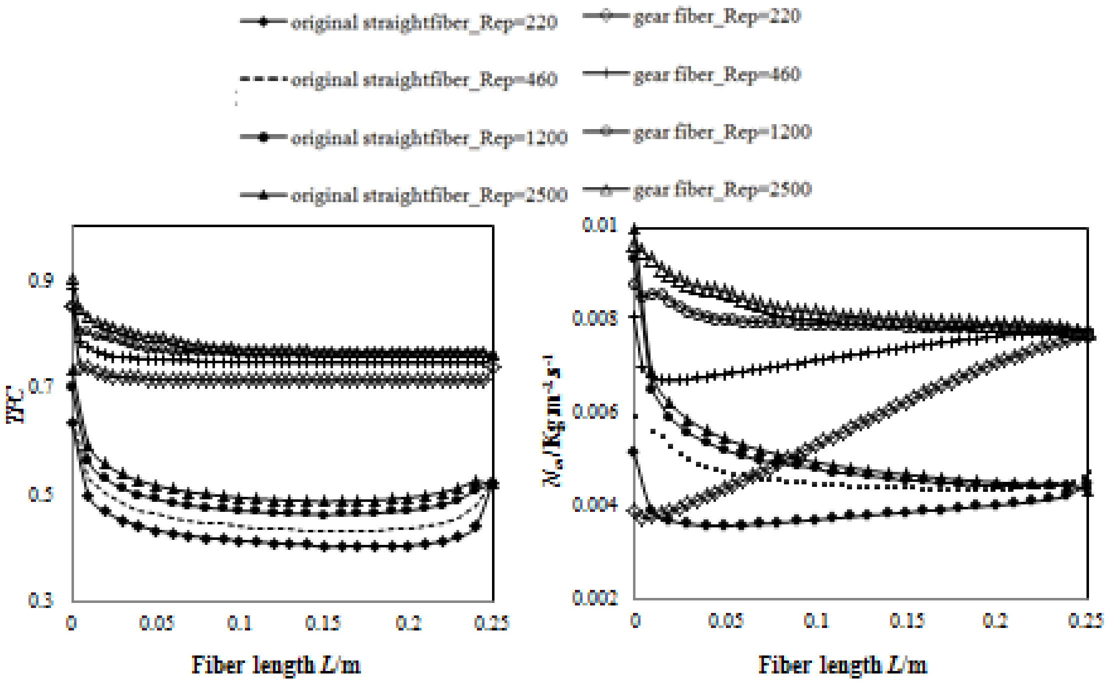

(a) *TPC* distributions

(b) N_m distributions

Fig. 11. Effect of permeate flow conditions (Re_p) for fibers of original straight and gear-shaped fibers ($C = 8.0\times10^{-7}$ kg·m^{-2}·s^{-1}·Pa^{-1} and C^*(gear) = 6.4×10^{-7} kg·m^{-2}·s^{-1}·Pa^{-1}, $L = 0.25$ m, $T_{fi} = 327.15$ K, T_{pi} = 293.85 K, $Re_f = 836$, $Re_p = 220$–2500)

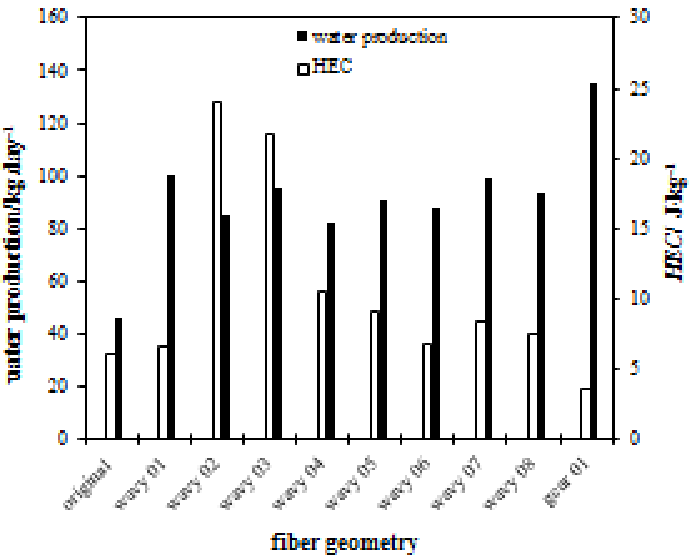

Fig. 12. Comparison of water production in multi-fiber modules with various fiber geometries (each module contains 100 fibers, $A=100A_s$, $C = 8.0\times10^{-7}$ kg·m^{-2}·s^{-1}·Pa^{-1} and C^*(gear) = 6.4×10^{-7} kg·m^{-2}·s^{-1}·Pa^{-1}, $L = 0.25$ m, $u_{fi} = 0.06$ m·s^{-1}, $u_{pi} = 0.417$ m·s^{-1}, $T_{fi} = 327.15$ K, $T_{pi} = 293.85$ K)

Table. 1. specification of various fiber geometric designs

Geometric pattern			Wavy geometry				Gear structure		Surface area
			Δx / mm	Δy / mm	Lx / mm	b	α	L_b mm	$A_{s} \times 10^{-4}$ m^2
1	Unmodified	Original	-	-	-	-	-	-	11.54
4	Wavy designs	Wavy 01 5.0/1.0	5.0	2.0	0	0.8			21.11
5		Wavy 02 2.5/2.0	2.5	2.0	0	0.5			41.39
6		Wavy 03 2.5/2.0	2.5	2.0	0	0.8			41.39
7		Wavy 04 1.25/1.0	1.25	1.0	0	0.7			27.30
8		Wavy 05 2.5/1.0	2.5	1.0	0	0.5			22.51
9		Wavy 06 alternate 5.0/1.0	5.0	2.0	5.0	0.8			16.34
		Wavy 07 alternate 1.25/1.0	1.25	1.0	1.25	0.7			19.42
		Wavy 08 alternate 2.5/1.0	2.5	1.0	2.5	0.5			17.03
10	Gear design	Gear-shaped	-	-	-	-	45	0.25	21.60

Note:

1. Δx and Δy are the dimensions of the wavy arch in x and r directions, respectively; Lx is the interval between two waves, b is the shape parameter representing the angle between the tangent of the circle and baseline. For example, a wavy design 2.5/1.0 indicates an conic arch of 2.5mm in x direction, 1.0mm in r direction from the baseline to the conic peak.
2. α is the interval angle between gears on the fiber, L_b is the dimension of a gear with square shape.

Table. 2. Summary of CFD mathematical models, boundary conditions and algorithms[38]

Governing transport equations	
Continuity equation	$\nabla \cdot \left(\rho \vec{v} \right) = 0$ (1)
Momentum transport equation*	$\nabla \cdot \left(\rho \vec{v} \vec{v} \right) = -\nabla p + \nabla \cdot \left(\bar{\bar{\tau}} \right) + \rho \vec{g}$ (2)
Energy conservation equation	$\nabla \cdot \left(\vec{v} \rho c_p T \right) = \nabla \cdot \left(k \nabla T \right) + S_h$ (3)
Boundary conditions	
Entrance of fluids (feed/ permeate)**	$U_{fi} = 0.06 - 0.283$ m·s^{-1}, $u_{pi} = 0.417$-2.265 m·s^{-1}, $T_{fi} = 327.15$ K, $T_{pi} = 293.85$ K
Exits of fluids (feed/permeate)	outlet pressure is 0.0 Pa (gauge pressure)
Membrane wall	no-slip condition, conjugate heat conduction: $q_f\big|_{r=R_{m,o}} = q_m\big|_{r=R_{m,o}}$ $\quad$ $q_m\big|_{r=R_{m,i}} = q_p\big|_{r=R_{m,i}}$ $T_f\big|_{r=R_{m,o}} = T_m\big|_{r=R_{m,o}}$ $\quad$ $T_p\big|_{r=R_{m,i}} = T_m\big|_{r=R_{m,i}}$
Solution algorithms	
Pressure-velocity coupling	SIMPLE (Semi-Implicit Method for Pressure Linked Equations)
Conservation equation discretization	QUICK (Quadratic Upstream Interpolation for Convective Kinetics)

*The momentum equation here only involves the motion in fluids, not the penetration through the membrane matrix. no-slip condition and no molecular transport across the membrane is applied in this model;

** typical experimental values

Table. 3. Summary of heat-transfer equations and definitions in MD [41]*

Heat transfer rate Q^{**}	$Q = Q_f = Q_p = Q_{MD} + Q_{HL}$	(4)
Latent heat flux q_{MD}	$q_{MD} = N_m \cdot \Delta H_{T_{fm}} = h_{MD} \cdot \left(T_{fm} - T_{pm} \right) = C \cdot \Delta P$	(5)
Local heat-transfer coefficient of the feed h_f	$h_f = \frac{q_f}{\left(T_f - T_{fm} \right)}$	(6)
Local heat-transfer coefficient of the permeate h_p	$h_p = \frac{q_p}{\left(T_{pm} - T_p \right)}$	(7)
Equivalent heat-transfer coefficient of the membrane h_m [41]	$h_m = \left(C\Delta P \cdot \Delta H_{T_{fm}} + \frac{k_m}{b} \frac{R_{fm}}{R_{ma}} \right) \frac{1}{\left(T_{fm} - T_{pm} \right)}$	(8)
Temperature-polarization coefficient (*TPC*) [2]	$TPC = \frac{T_{fm} - T_{pm}}{T_f - T_p}$	(9)
Hydraulic energy consumption (*HEC*)	$HEC = \frac{\Delta P_{fluid} \cdot V}{N_m \cdot A}$	(10)

*The MD related mass- and heat-transfer equations here only involves in the CFD data postprocessing.

**The heat-transfer rate $Q = q \times A$